Multistability in planar liquid crystal wells

Chong Luo,* Apala Majumdar,† and Radek Erban‡
Mathematical Institute, University of Oxford, 24-29 St. Giles', Oxford OX1 3LB, United Kingdom
(Received 4 November 2011; published 8 June 2012)

A planar bistable liquid crystal device, reported in Tsakonas *et al.* [Appl. Phys. Lett. **90**, 111913 (2007)], is modeled within the Landau-de Gennes theory for nematic liquid crystals. This planar device consists of an array of square micrometer-sized wells. We obtain six different classes of equilibrium profiles and these profiles are classified as *diagonal* or *rotated* solutions. In the strong anchoring case, we propose a Dirichlet boundary condition that mimics the experimentally imposed *tangent boundary conditions*. In the weak anchoring case, we present a suitable surface energy and study the multiplicity of solutions as a function of the anchoring strength. We find that diagonal solutions exist for all values of the anchoring strength $W \geqslant 0$, while rotated solutions only exist for $W \geqslant W_c > 0$, where W_c is a critical anchoring strength that has been computed numerically. We propose a dynamic model for the switching mechanisms based on only dielectric effects. For sufficiently strong external electric fields, we numerically demonstrate diagonal-to-rotated and rotated-to-diagonal switching by allowing for variable anchoring strength across the domain boundary.

DOI: 10.1103/PhysRevE.85.061702 PACS number(s): 42.79.Kr, 61.30.Hn, 61.30.Cz

I. INTRODUCTION

Liquid crystal science has grown tremendously over the last four decades for fundamental scientific reasons and for widespread liquid crystalline applications in modern industry and technology, e.g., in display devices [1], in novel functional materials, and in biological sensors [2]. The simplest liquid crystal phase is the nematic phase wherein the constituent rodlike molecules have a degree of long-range orientational ordering and, hence, tend to align along certain locally preferred directions [3]. The existence of such distinguished directions in nematic liquid crystals and their resulting anisotropic optical properties make nematics suitable working materials for optical devices such as displays. Recently, there has been considerable interest in the development of bistable liquid crystal displays [4–6]. Bistable displays can support two or more stable, optically contrasting, liquid crystal states, so that power is only required to switch between the optically contrasting states, but not to maintain a static image. Thus, bistable displays offer the promise of a new generation of larger, economical, and high-resolution displays that are very lucrative for industry.

Bistable displays typically use a combination of complex surface morphologies and surface treatments to stabilize multiple liquid crystal states [5–7]. Examples of bistable displays include the two-dimensional zenithally bistable nematic (ZBN) device [7] and the three-dimensional post aligned bistable nematic (PABN) device [6]. The ZBN device consists of a liquid crystal layer sandwiched between two solid surfaces where the bottom surface is featured by a complex wedge-shaped grating. Both surfaces are treated to induce *homeotropic* (*normal*) boundary conditions and the ZBN cell supports two static stable states: the defect-free vertically aligned nematic (VAN) state and the hybrid aligned nematic (HAN) state which is distinguished by defects near the wedge-shaped grating [7]. The PABN cell has a three-dimensional structure with a liquid crystal layer sandwiched between two solid substrates, and the bottom substrate is featured by an array of microscopic posts. Unlike the ZBN cell, the boundary conditions for the PABN cell are of a mixed type. The top substrate is treated to induce homeotropic boundary conditions, while the bottom substrate and the post surfaces are treated to have *tangent* (*planar*) boundary conditions. Experimental observations and optical modeling suggest that there are at least two competing static stable states: the opaque *tilted* state and the transparent *planar* state [6].

In this paper, we focus on the two-dimensional bistable liquid crystal device investigated both experimentally and numerically by Tsakonas *et al.* [8]. This device consists of an array of square wells filled with nematic liquid crystal material. The well surfaces are treated to induce *tangent boundary conditions*, i.e., the liquid crystal molecules in contact with the well surfaces are constrained to be in the plane of the surfaces. When viewed between crossed polarizers, the authors observe two classes of stable equilibria in this geometry: *diagonal* states where the liquid crystal molecules align along the square diagonals and *rotated* states where the direction of alignment rotates by π across the width of the cell. The experimental results are also accompanied by modeling in the Landau-de Gennes framework [8]. Similar liquid crystal square wells have also been studied in [9], where diagonal solutions have been observed. In [10], the interrelationship between the well aspect ratio and the boundary conditions (planar or homeotropic) has been investigated both experimentally and numerically.

In the experiments of Tsakonas *et al.* [8], the height of the well is less than half the cross-sectional length of the square well, inducing the molecules to lie primarily in the plane of the bottom cross section. Hence, a two-dimensional model should suffice to capture the important configurational details of this device since this is equivalent to neglecting structural variations across the height of the cell and focusing on the structural variations across the square cross section. Keeping this in mind, we build on the results in [8] within the Landau-de Gennes framework [3] and model the device on a two-dimensional square or rectangular domain. We

*luo@maths.ox.ac.uk
†majumdar@maths.ox.ac.uk
‡erban@maths.ox.ac.uk

first formulate the modeling problem in terms of a Dirichlet boundary-value problem and introduce the concept of an *optimal* Dirichlet boundary condition. There are multiple choices of Dirichlet boundary conditions consistent with the experimentally imposed tangent boundary conditions, and we formulate the *optimal* Dirichlet boundary condition as the solution of a variational problem. We then consider the more physically realistic weak anchoring situation where we relax the Dirichlet boundary condition and impose an appropriate surface energy characterized by an anchoring strength W. The resulting mathematical problem is well posed, yields physically realistic equilibria for all values of the anchoring strength $W > 0$, and the weak anchoring equilibria converge to the strong anchoring equilibria in the limit of infinite anchoring. We numerically compute bifurcation diagrams for the equilibria in the weak anchoring case and study the multiplicity of stable equilibria as a function of the anchoring strength. We numerically find six different classes of solutions, two of which are labeled as *diagonal* and four of which are labeled as *rotated* based on their alignment structures. The diagonal solutions exist for all $W \geqslant 0$, whereas the rotated solutions only exist for anchoring strengths above a certain critical value $W_c > 0$. We estimate this critical anchoring strength in terms of the material parameters and find that the system is bistable or multistable for $W \geqslant W_c$.

We propose a simple dynamic model based on the gradient flow approach for the switching characteristics of this device. This model only relies on dielectric effects and we do not incorporate flexoelectricity, unlike other models in the existing literature [11]. Our dynamic model does not account for viscous dissipation or fluid-flow effects, but simply gives a qualitative description of a mechanism that can drive the switching procedure. To achieve switching from diagonal to rotated and vice versa, we make the anchoring strength on one of the square edges much weaker than that on the remaining three square edges and we apply a uniform electric field along the square diagonals.

The paper is organized as follows. In Sec. II, we review the Landau-de Gennes $\boldsymbol{Q}$-tensor theory for liquid crystals. In Sec. III, we study the strong anchoring problem. In Sec. IV, we study the weak anchoring problem and present bifurcation diagrams for the corresponding equilibria as a function of the anchoring strength. In Sec. V, we demonstrate a switching mechanism between the competing stable states under the action of an external electric field. Finally, in the Appendix, we elaborate on the numerical methods.

II. TWO-DIMENSIONAL LANDAU-DE GENNES THEORY

The Oseen-Frank theory is the simplest continuum theory for nematic liquid crystals, based on the assumption of strict uniaxiality (a single distinguished direction of molecular alignment) and a constant degree of orientational ordering [12]. In the Oseen-Frank framework, the liquid crystal configuration is modeled by a unit-vector field $\boldsymbol{n}$ (often referred to as *director* because of the $\boldsymbol{n} \to -\boldsymbol{n}$ symmetry), which represents the locally preferred direction of molecular alignment. The Oseen-Frank theory assigns a free energy to every admissible $\boldsymbol{n}$ and, working in the simplest one-constant approximation, the Oseen-Frank energy reduces to the well-known Dirichlet energy [13],

$$\mathcal{E}_{\mathrm{OF}}[\boldsymbol{n}] := \int_{\Omega} \frac{1}{2} K |\nabla \boldsymbol{n}|^2 dA, \tag{1}$$

where $\Omega \subset \mathbb{R}^2$ is the physical domain, dA is the corresponding area element, and $K > 0$ is an elastic constant. To have finite Oseen-Frank energy (1), the admissible $\boldsymbol{n}$ must belong to the Sobolev space $H^1(\Omega, S^1)$, which is the space of unit-vector fields with square-integrable first derivatives [14].

However, the Oseen-Frank theory is not well suited to model the planar square (or rectangular) bistable device reported in Tsakonas *et al.* [8]. As stated in the previous section, the tangent boundary conditions constrain the liquid crystal molecules in contact with the well surfaces to be in the plane of the well surfaces [15]. Taking the modeling domain to be a square or a rectangle and working in the Oseen-Frank framework, this implies that the unit-vector field $\boldsymbol{n}$ is constrained to be tangent to the square or rectangle edges, i.e., $\boldsymbol{n}$ is aligned horizontally on the horizontal edges and vertically on the vertical edges. Thus, $\boldsymbol{n}$ is necessarily discontinuous at the vertices where two or more edges meet. However, it has been shown in [16] that unit-vector fields with the jump discontinuous Dirichlet boundary condition do not belong to $H^1(\Omega)$ for $\Omega \subset \mathbb{R}^2$, and hence have infinite Oseen-Frank energy (1). This difficulty can be resolved by introducing an order parameter that can vanish at defect locations; i.e., we need to relax the assumption of constant orientational ordering in the Oseen-Frank framework.

We model the planar bistable device by a rectangular domain,

$$\Omega = \{(x,y) \in \mathbb{R}^2 : x \in [0,L], y \in [0, a_r \times L]\}, \tag{2}$$

where L is the width of the rectangle and a_r is the aspect ratio. We work within the Landau-de Gennes framework [3, 17,18], whereby the liquid crystal configuration is modeled by a symmetric traceless tensor $\boldsymbol{Q}$. In the two-dimensional (2D) case, the $\boldsymbol{Q}$ tensor can be written as

$$\boldsymbol{Q} = s(2\boldsymbol{n} \otimes \boldsymbol{n} - I), \tag{3}$$

where $\boldsymbol{n} = \boldsymbol{n}(x,y)$ is an eigenvector, $s = s(x,y)$ is a scalar order parameter that measures the degree of orientational ordering about $\boldsymbol{n}$, and I is the 2×2 identity matrix [13]. Unlike the Oseen-Frank theory, the order parameter s in the $\boldsymbol{Q}$-tensor model varies across the modeling domain and, in particular, vanishes at the vertices as required.

The $\boldsymbol{Q}$ tensor is invariant under the transformation $\boldsymbol{n} \to -\boldsymbol{n}$ and preserves the head-to-tail symmetry of the nematic molecules [19]. Since $\boldsymbol{Q}$ is symmetric and traceless, we can write it in the following matrix form:

$$\boldsymbol{Q} = \begin{pmatrix} Q_{11} & Q_{12} \\ Q_{12} & -Q_{11} \end{pmatrix}. \tag{4}$$

Any 2D unit-vector field $\boldsymbol{n}$ can be written in terms of an angle θ in the xy plane,

$$\boldsymbol{n}(x,y) = [\cos\theta(x,y), \sin\theta(x,y)]. \tag{5}$$

Then one can readily check that

$$Q_{11} = s\cos(2\theta), \tag{6}$$

$$Q_{12} = s\sin(2\theta). \tag{7}$$

Also, we have

$$\operatorname{tr}\boldsymbol{Q} = \operatorname{tr}\boldsymbol{Q}^3 = 0, \tag{8}$$

$$\operatorname{tr}\boldsymbol{Q}^2 = 2s^2. \tag{9}$$

In the absence of external fields and surface effects, the Landau-de Gennes energy functional is given by

$$\mathcal{E}_{\mathrm{LDG}} = \mathcal{E}_{el} + \mathcal{E}_B, \tag{10}$$

where $\mathcal{E}_{el}$ is an elastic energy and $\mathcal{E}_B$ is the bulk energy [18,19]. In the simplest one-constant approximation case, the elastic energy is taken to be

$$\mathcal{E}_{el}[\boldsymbol{Q}] := \int_\Omega \frac{L_{el}}{2}|\nabla\boldsymbol{Q}|^2 dA, \tag{11}$$

where $L_{el} > 0$ is an elastic constant [3,19]. The bulk energy depends on the scalar invariants of $\boldsymbol{Q}$,

$$\mathcal{E}_B[\boldsymbol{Q}] := \int_\Omega \overline{\alpha}(T)\operatorname{tr}\boldsymbol{Q}^2 - \frac{b^2}{3}\operatorname{tr}\boldsymbol{Q}^3 + \frac{c^2}{4}(\operatorname{tr}\boldsymbol{Q}^2)^2 dA,$$

where $\overline{\alpha}(T) = \gamma(T - T^*)$ with $\gamma > 0$, T denotes the absolute temperature, and T^* is a characteristic temperature below which the disordered isotropic phase loses its stability [19]. Further, b^2 and c^2 are positive material-dependent constants [3,18]. We work in the low-temperature regime and, in this case, for a fixed temperature $T < T^*$, we can write the bulk energy as

$$\mathcal{E}_B[\boldsymbol{Q}] = \int_\Omega -\frac{\alpha^2}{2}\operatorname{tr}\boldsymbol{Q}^2 - \frac{b^2}{3}\operatorname{tr}\boldsymbol{Q}^3 + \frac{c^2}{4}(\operatorname{tr}\boldsymbol{Q}^2)^2 dA,$$

where $\alpha^2 > 0$ is a temperature-dependent and material-dependent constant. For a two-dimensional problem, one can directly verify that

$$\mathcal{E}_{el}[\boldsymbol{Q}] = \int_\Omega L_{el}(|\nabla Q_{11}|^2 + |\nabla Q_{12}|^2)dA, \tag{12}$$

and

$$\mathcal{E}_B[\boldsymbol{Q}] = \int_\Omega c^2 s^4 - \alpha^2 s^2 dA. \tag{13}$$

The bulk energy $\mathcal{E}_B$ achieves its minimum at

$$s \equiv s_0 = \sqrt{\frac{\alpha^2}{2c^2}}. \tag{14}$$

We define

$$\varepsilon^2 := \frac{1}{c^2}. \tag{15}$$

Then, $\mathcal{E}_B$ can be rewritten as

$$\mathcal{E}_B[\boldsymbol{Q}] = \int_\Omega \frac{1}{\varepsilon^2}\left(s^2 - s_0^2\right)^2 - \frac{s_0^4}{\varepsilon^2} dA. \tag{16}$$

Therefore up to an additive constant independent of s and θ, the Landau-de Gennes energy is given by

$$\mathcal{E}_{\mathrm{LDG}}[\boldsymbol{Q}] = \int_\Omega L_{el}(|\nabla Q_{11}|^2 + |\nabla Q_{12}|^2) + \frac{1}{\varepsilon^2}\left(Q_{11}^2 + Q_{12}^2 - s_0^2\right)^2 dA. \tag{17}$$

In the strong anchoring case, the eigenvector $\boldsymbol{n}$ in (3) is constrained to be strictly tangent to the edges of the rectangular domain, i.e., $\boldsymbol{n} = \pm\mathbf{e}_x$ on the horizontal edges and $\boldsymbol{n} = \pm\mathbf{e}_y$ on the vertical edges, where $\mathbf{e}_x$ and $\mathbf{e}_y$ are the unit vectors in the x- and y-coordinate directions, respectively. These boundary conditions are encoded by a Dirichlet boundary condition $(Q_{11}, Q_{12}) = \boldsymbol{g}$, for some Lipschitz continuous $\boldsymbol{g}$, and we will prescribe an appropriate form of $\boldsymbol{g}$ in the next section.

In the weak anchoring case, the Dirichlet boundary condition $(Q_{11}, Q_{12}) = \boldsymbol{g}$ is replaced by a surface anchoring energy which favors the tangent boundary conditions. We have studied three different candidates for the surface anchoring energy. The first choice is

$$\mathcal{E}_A[\boldsymbol{Q}] := \int_{\partial\Omega} \frac{W\boldsymbol{\nu}\cdot\boldsymbol{Q}\boldsymbol{\nu}}{\sqrt{Q_{11}^2 + Q_{12}^2}} da, \tag{18}$$

where da is the line element on $\partial\Omega$, $\boldsymbol{\nu}$ is the outward unit-normal vector on $\partial\Omega$, and $W = W(x,y)$ is the nonuniform anchoring strength on $\partial\Omega$ which might take different values across the boundary. We take W to be a constant in this paper, unless otherwise specified as in the section on switching characteristics. The energy (18) is equivalent to the widely used Rapini-Papoular surface energy,

$$\int_{\partial\Omega} 2W\sin^2(\theta - \theta_0) da, \tag{19}$$

where θ_0 denotes the preferred orientation on the boundary [20]. However, this surface energy has the following shortcomings: (i) the energy density is discontinuous at $(Q_{11}, Q_{12}) = (0,0)$, and (ii) for large $W > 0$, we are numerically unable to compute the corresponding equilibria because of convergence problems. A second choice for the surface anchoring energy is

$$\mathcal{E}_A[\boldsymbol{Q}] := \int_{\partial\Omega} W\boldsymbol{\nu}\cdot\boldsymbol{Q}\boldsymbol{\nu} da, \tag{20}$$

as has been used in [8]. For a fixed $\varepsilon > 0$, the order parameter s becomes unbounded in the limit $W \to \infty$, leading to nonphysical solutions. The third and the most suitable choice is the Durand-Nobili surface anchoring energy proposed in [21],

$$\mathcal{E}_A[\boldsymbol{Q}] := \int_{\partial\Omega} W|(Q_{11}, Q_{12}) - \boldsymbol{g}|^2 da, \tag{21}$$

where $\boldsymbol{g}$ is the Dirichlet boundary condition for the strong anchoring problem. For a suitable choice of $\boldsymbol{g}$, this surface energy enjoys the following advantages, as will be demonstrated in the subsequent numerical results: (i) we can find equilibrium solutions for arbitrarily large $W > 0$, (ii) the order parameter s is bounded in the limit $W \to \infty$, and (iii) as $W \to \infty$, the weak anchoring solutions converge to the corresponding strong anchoring solutions in $H^1(\Omega, \mathbb{R}^2)$. The properties of the three different surface anchoring energies (18), (20), and (21) are summarized in Table I.

TABLE I. Comparison of the different surface energies (18), (20), and (21).

Model	Existence for large W	Boundedness of s	Convergence to strong anchoring
(18)	×	√	×
(20)	√	×	×
(21)	√	√	√

To model the switching dynamics of this bistable device, an external electric field must be included in the formulation. In the Landau-de Gennes framework, the electrostatic energy is given by

$$\mathcal{E}_E[\boldsymbol{Q}] := \int_\Omega -\frac{1}{2}\epsilon_0(\boldsymbol{\epsilon}\boldsymbol{E})\cdot\boldsymbol{E} - \boldsymbol{P}_s\cdot\boldsymbol{E}\,dA, \tag{22}$$

where $\boldsymbol{E}$ is the electric field vector, $\boldsymbol{P}_s$ is the spontaneous polarization vector, $\boldsymbol{\epsilon}$ is the dielectric tensor and can be approximated by $\boldsymbol{\epsilon} = \triangle\epsilon^*\boldsymbol{Q} + \bar{\epsilon}I$, ϵ_0 is the vacuum permittivity, and $\triangle\epsilon^*$, $\bar{\epsilon}$ are material-dependent constants [19]. In particular, $\triangle\epsilon^*$ is the dielectric anisotropy, and we work with materials that have positive dielectric anisotropy in what follows. In this paper, we assume that the flexoelectric effect (the P_s term) is negligible compared to the dielectric effect, and the electrostatic energy then simplifies to

$$\mathcal{E}_E[\boldsymbol{Q}] = \int_\Omega -C_0(\boldsymbol{Q}\boldsymbol{E})\cdot\boldsymbol{E}\,dA, \tag{23}$$

with $C_0 = \frac{1}{2}\epsilon_0\triangle\epsilon^*$. Let $\boldsymbol{E} = |\boldsymbol{E}|(\cos\theta_E, \sin\theta_E)$ for some angle θ_E; then the electrostatic energy in (23) reduces to

$$\mathcal{E}_E[\boldsymbol{Q}] = \int_\Omega -C_0|\boldsymbol{E}|^2[Q_{11}\cos(2\theta_E) + Q_{12}\sin(2\theta_E)]dA. \tag{24}$$

The total energy is the sum of the elastic energy $\mathcal{E}_{el}$, the bulk energy $\mathcal{E}_B$, the surface anchoring energy $\mathcal{E}_A$, and the electrostatic energy $\mathcal{E}_E$,

$$\begin{aligned}\mathcal{E}[\boldsymbol{Q}] = &\int_\Omega L_{el}(|\nabla Q_{11}|^2 + |\nabla Q_{12}|^2) + \frac{1}{\varepsilon^2}\left(Q_{11}^2 + Q_{12}^2 - s_0^2\right)^2 dA\\ &+ \int_{\partial\Omega} W|(Q_{11}, Q_{12}) - \boldsymbol{g}|^2 da\\ &+ \int_\Omega -C_0|\boldsymbol{E}|^2[Q_{11}\cos(2\theta_E) + Q_{12}\sin(2\theta_E)]dA.\end{aligned} \tag{25}$$

Before we proceed with the analysis and numerical computations, we nondimensionalize the system as follows. Take the reference domain to be $\tilde{\Omega} = [0,1]\times[0,a_r]$ and let $\tilde{x} = x/L$, $\tilde{y} = y/L$. Define variables

$$(\tilde{Q}_{11}, \tilde{Q}_{12}) := (Q_{11}, Q_{12})/s_0, \tag{26}$$

$$\tilde{\boldsymbol{g}} := \boldsymbol{g}/s_0, \tag{27}$$

and

$$\tilde{\varepsilon} := \frac{\varepsilon\sqrt{L_{el}}}{L}, \tag{28}$$

$$\tilde{W} := \frac{WL}{L_{el}}, \tag{29}$$

$$\tilde{E} := \frac{L|\boldsymbol{E}|}{s_0}\sqrt{\frac{|C_0|}{L_{el}}}. \tag{30}$$

Then, the total energy $\mathcal{E}$ can be written in terms of these dimensionless variables:

$$\begin{aligned}\frac{1}{s_0^2 L_{el}}\mathcal{E}[\boldsymbol{Q}] = &\int_{\tilde{\Omega}}(|\nabla\tilde{Q}_{11}|^2 + |\nabla\tilde{Q}_{12}|^2) + \frac{1}{\tilde{\varepsilon}^2}\left(\tilde{Q}_{11}^2 + \tilde{Q}_{12}^2 - 1\right)^2 d\tilde{A}\\ &+ \int_{\partial\tilde{\Omega}}\tilde{W}|(\tilde{Q}_{11}, \tilde{Q}_{12}) - \tilde{\boldsymbol{g}}|^2 d\tilde{a}\\ &+ \int_{\tilde{\Omega}} -\mathrm{sgn}(C_0)\tilde{E}^2[\tilde{Q}_{11}\cos(2\theta_E)\\ &+ \tilde{Q}_{12}\sin(2\theta_E)]d\tilde{A},\end{aligned} \tag{31}$$

where $d\tilde{A}$ and $d\tilde{a}$ are the area element in $\tilde{\Omega}$ and the line element on $\partial\tilde{\Omega}$, respectively. In what follows, we work at a fixed temperature with the dimensionless energy $\tilde{\mathcal{E}} := \mathcal{E}/(s_0^2 L_{el})$.

Some typical values of the physical parameters are $1/\varepsilon^2 = 1\times10^6\ \mathrm{N\,m^{-1}}$, $L_{el} = 10^{-11}\ \mathrm{N\,m}$, $s_0 = 0.6$, $L = 8\times10^{-5}$ m, and $W = 2\times10^{-3}$ N, as given in [8]. By (28), the dimensionless parameter $\tilde{\varepsilon}$ is about 6.6×10^{-5}. Since $\tilde{\varepsilon}$ is so small, we can view the bulk energy density $\frac{1}{\tilde{\varepsilon}^2}(\tilde{Q}_{11}^2 + \tilde{Q}_{12}^2 - 1)^2$ as a penalty term that enforces $\tilde{Q}_{11}^2 + \tilde{Q}_{12}^2 = 1$ a.e. in $\tilde{\Omega}$. Similarly, by Eq. (29), the dimensionless anchoring strength $\tilde{W}$ is about 1.6×10^4. For simplicity, we remove the tildes in the following sections, and all of the variables and parameters are dimensionless unless otherwise specified.

III. STRONG ANCHORING

In the strong anchoring case, the dimensionless energy functional is

$$\mathcal{E}[\boldsymbol{Q}] = \int_\Omega(|\nabla Q_{11}|^2 + |\nabla Q_{12}|^2) + \frac{1}{\varepsilon^2}\left(Q_{11}^2 + Q_{12}^2 - 1\right)^2 dA, \tag{32}$$

accompanied by a Dirichlet boundary condition $(Q_{11}, Q_{12}) = \boldsymbol{g}$. We note that (32) is precisely the Ginzburg-Landau energy functional for superconductors, which has been extensively studied in the literature [13,22].

The boundary condition $\boldsymbol{g}$ has to be carefully chosen, as we now describe. In the strong in-plane anchoring situation, the eigenvector $\boldsymbol{n}$ in (3) is constrained to be strictly tangent to the domain edges. On the top and bottom edges, $\theta = 0$ or π and, hence, by (6) and (7), we have

$$Q_{11} = s, \tag{33}$$

$$Q_{12} = 0, \tag{34}$$

where $s^2 = Q_{11}^2 + Q_{12}^2$. On the left and right edges, $\theta = \pi/2$ or $-\pi/2$, and thus

$$Q_{11} = -s, \tag{35}$$

$$Q_{12} = 0. \tag{36}$$

We take s to be strictly non-negative on the boundary. Therefore, solutions of the strong anchoring problem satisfy

the following conditions:

$$Q_{11} \geqslant 0 \quad \text{on horizontal edges,} \tag{37}$$

$$Q_{11} \leqslant 0 \quad \text{on vertical edges, and} \tag{38}$$

$$Q_{12} = 0 \quad \text{on } \partial\Omega. \tag{39}$$

Any Lipschitz continuous function $\boldsymbol{g} : \partial\Omega \to \mathbb{R}^2$ that satisfies the conditions (37)–(39) results in a well-posed energy minimization problem. For any Lipschitz continuous $\boldsymbol{g}$, the admissible space

$$\mathcal{A}_{\boldsymbol{g}} = \{\boldsymbol{u} \in H^1(\Omega,\mathbb{R}^2) : \boldsymbol{u} = \boldsymbol{g} \text{ on } \partial\Omega\} \tag{40}$$

is nonempty [23]. Furthermore, since the energy functional (32) is coercive and convex in ∇Q, we are guaranteed the existence of a global energy minimizer in $\mathcal{A}_{\boldsymbol{g}}$ [24].

For any fixed Dirichlet boundary condition $\boldsymbol{g}$, we can use standard tools in the calculus of variations to show that local minimizers (Q_{11}, Q_{12}) of the energy functional (32) in the admissible set $\mathcal{A}_{\boldsymbol{g}}$ are solutions of the following integral equations:

$$0 = \int_\Omega \nabla Q_{11}\nabla v_{11} + \frac{2}{\varepsilon^2}\left(Q_{11}^2 + Q_{12}^2 - 1\right)Q_{11}v_{11}dA \quad \forall\, v_{11} \in H_0^1(\Omega), \tag{41}$$

$$0 = \int_\Omega \nabla Q_{12}\nabla v_{12} + \frac{2}{\varepsilon^2}\left(Q_{11}^2 + Q_{12}^2 - 1\right)Q_{12}v_{12}dA \quad \forall\, v_{12} \in H_0^1(\Omega), \tag{42}$$

where the test functions v_{11} and v_{12} are in the Sobolev space $H_0^1(\Omega)$ [25] since this is a Dirichlet problem and the boundary values of Q_{11} and Q_{12} are given. We discretize the system and solve it using finite-element methods [26]. The details of the numerical methods can be found in the Appendix.

We find that for each fixed Lipschitz continuous $\boldsymbol{g}$, there are typically six distinct equilibrium solutions. We categorize these six solutions as either *diagonal* or *rotated*, according to their director profiles. There are two diagonal solutions, which we label as D1 and D2, respectively, and four rotated solutions, which we label as R1, R2, R3, and R4, respectively. The director profiles of these six solutions are shown in Fig. 1. We find that among the six solutions, the two diagonal solutions are energetically degenerate while the four rotated solutions are energetically degenerate. However, the rotated solutions have slightly higher energies than those of the corresponding diagonal solutions.

In what follows, we choose an appropriate Lipschitz continuous $\boldsymbol{g}$ as the fixed boundary condition for the Dirichlet problem to be studied in this paper. For each fixed ε, a different choice of the Dirichlet boundary condition $\boldsymbol{g}$ yields a different set of diagonal and rotated solutions. There is an optimal Dirichlet boundary condition $\boldsymbol{g}_{\mathrm{D1}}$ whose D1-diagonal solution has the minimum energy in the space of all D1-type diagonal solutions. Similarly, there is an optimal Dirichlet boundary condition for each of the other five solution types too. Let (Q_{11}, Q_{12}) be a local minimizer of (32) in the admissible space,

$$\mathcal{A} = \{(u_1,u_2) \in H^1(\Omega,\mathbb{R}^2) : u_2 = 0 \text{ on } \partial\Omega\}. \tag{43}$$

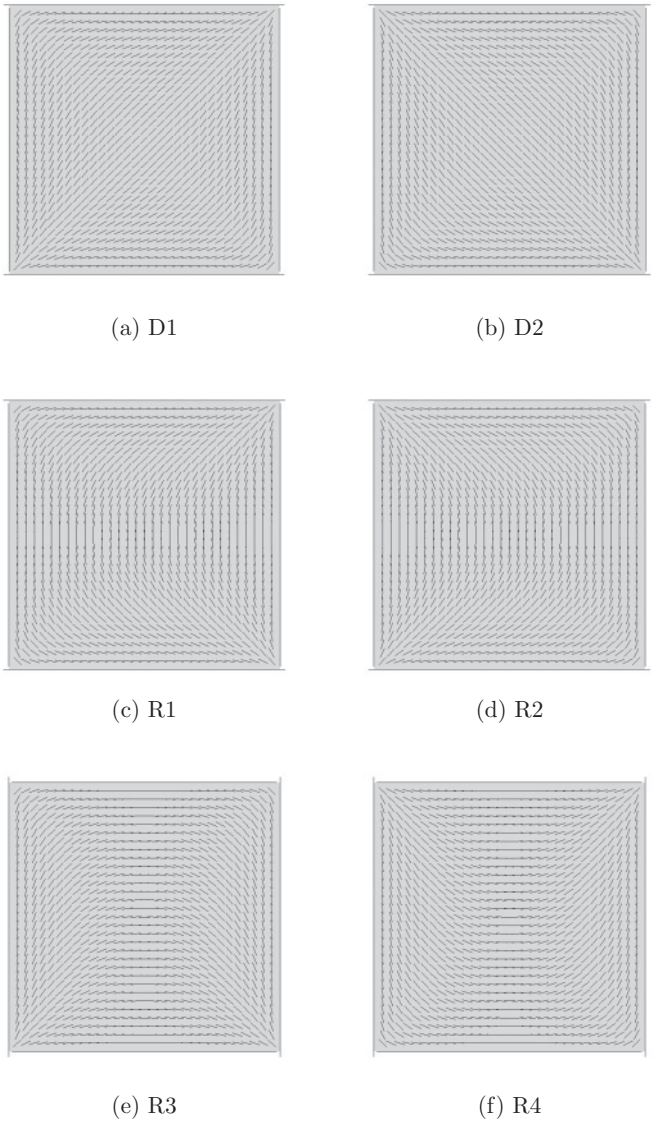

(a) D1 (b) D2 (c) R1 (d) R2 (e) R3 (f) R4

FIG. 1. The six types of solutions of (41) and (42).

Then, (Q_{11}, Q_{12}) satisfies the following integral equations:

$$0 = \int_\Omega \nabla Q_{11}\nabla v_{11} + \frac{2}{\varepsilon^2}\left(Q_{11}^2 + Q_{12}^2 - 1\right)Q_{11}v_{11}dA \quad \forall\, v_{11} \in H^1(\Omega), \tag{44}$$

$$0 = \int_\Omega \nabla Q_{12}\nabla v_{12} + \frac{2}{\varepsilon^2}\left(Q_{11}^2 + Q_{12}^2 - 1\right)Q_{12}v_{12}dA \quad \forall\, v_{12} \in H_0^1(\Omega), \tag{45}$$

where the test function v_{12} is in $H_0^1(\Omega)$ while v_{11} is in $H^1(\Omega)$ because the boundary value of Q_{12} is fixed and that of Q_{11} is not [note the difference between Eqs. (44) and (45) and (41) and (42)]. Solutions of (44) and (45) are defined to be *optimal solutions*, and the corresponding traces on $\partial\Omega$ are labeled as *optimal boundary conditions*.

Defects have a straightforward interpretation within the two-dimensional Landau-de Gennes framework. Any locally or globally stable $\boldsymbol{Q}$ in our admissible space is analytic but its eigenvectors can have discontinuities. Since $\boldsymbol{Q}$ is analytic, $\boldsymbol{Q} = 0$ at any such point of discontinuity. In what follows, we

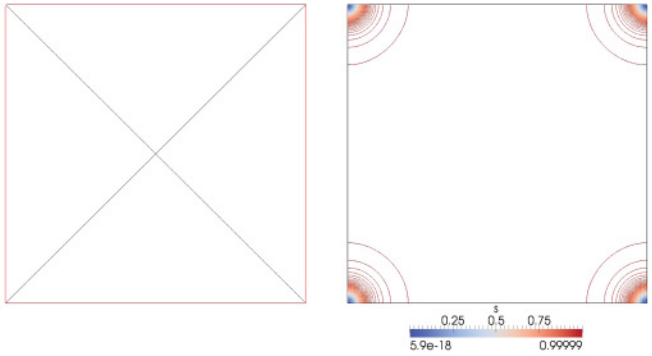

(a) Defects of the optimal D1-solution are exactly at the four corners.

(b) Contour lines of the order parameter of the optimal D1-solution.

FIG. 2. (Color online) (a) The two diagonal (blue) lines are where $Q_{11} = 0$, and the domain boundary (red) is where $Q_{12} = 0$. The defects are at the intersections of the two kinds of curves. (b) The contour lines from near the corners to the center correspond to increasing values of s with a step size of $\triangle s = 0.01$. The blank region in the center has s values in $[0.99,1]$. In both figures, the domain is the reference domain with width 1 (dimensionless). Parameters: $\varepsilon = 0.02$, mesh size $N = 256$, and $a_r = 1$.

locate defects as isotropic points of the $\boldsymbol{Q}$ tensor. In Fig. 2, we plot the defect locations (where the tensor $\boldsymbol{Q} = 0$) and order parameter contour lines of the optimal D1 solution. Figure 2(a) shows that the defects of the optimal D1 solution are located at the four corners of the square domain. Figure 2(b) shows that the contour lines in a neighborhood of the four corners are almost circular, suggesting a radial profile for s in these regions. That is, close to any corner P, we have $s(\boldsymbol{x},\varepsilon) = s(|\boldsymbol{x} - P|,\varepsilon)$. In Fig. 3, we plot the order parameter s of optimal D1 solutions as a function of $|\boldsymbol{x}|/(50\varepsilon)$ for $\boldsymbol{x}$ near the lower-left corner, for four different values of ε. We can see that the four curves are almost identical. This suggests a

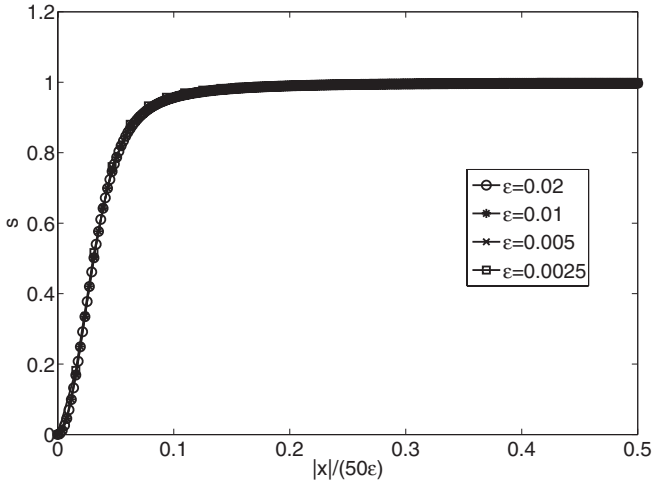

FIG. 3. The plots of $s = s[|\boldsymbol{x}|/(50\varepsilon)]$ with $\varepsilon = 0.02, 0.01, 0.005$, and 0.0025 for $\boldsymbol{x}$ close to the lower-left corner in the optimal D1 solutions. Parameters: mesh size $N = 512$ and $a_r = 1$.

functional form

$$s(\boldsymbol{x},\varepsilon) = s\left(\frac{|\boldsymbol{x} - P|}{50\varepsilon}\right), \tag{46}$$

in the vertex vicinity. Therefore, if we choose any cutoff value $0 < C \ll 1$, and define a defect core to be the localized region where $s(\boldsymbol{x},\varepsilon) < C$, then the defect core sizes are proportional to ε. Additionally, Eq. (46) suggests that the order parameter of the defect cores of optimal D1 solutions for different values of ε can actually be mapped to one another by a simple scaling law. In terms of the physical variables, the defect core sizes are proportional to $\tilde{\varepsilon}L$, which, by (28) and (15), is equal to $\sqrt{L_{el}/c^2}$. In other words, the defect size (for a fixed temperature) is proportional to a characteristic length scale $\sqrt{L_{el}/c^2}$ and is independent of the size of the square well (for macroscopic wells).

Figure 4 shows the defect locations and order parameter contour lines for the optimal R2 solution. Figure 4(a) shows that the defects for the optimal R2 solution are close to, but not exactly, at the four corners of the square domain. More precisely, the defects are at $(0,\kappa)$, $(0,1-\kappa)$, $(1,\kappa)$, and $(1,1-\kappa)$ for some $\kappa > 0$. Numerical results show that κ tends to zero as ε tends to zero. For example, for $\varepsilon = 0.02$, we have the estimate $1/256 < \kappa < 3/512$, while for $\varepsilon = 0.01$, we have the estimate $0 < \kappa < 1/512$. As stated at the end of Sec. II, typical values are $\varepsilon \sim 10^{-5}$ and, hence, we expect that the defects of the corresponding optimal R2 solution will be pinned to the vertices of the square domain. Figure 4(b) shows that unlike the optimal D1 solutions, the order parameter contour lines of the optimal R2 solution are not perfectly circular.

We briefly comment on the notion of an optimal boundary condition. For small ε, the optimal boundary conditions enforce $s = 1$ almost everywhere on the square or rectangle boundary, except for at the vertices where $s = 0$. The optimal

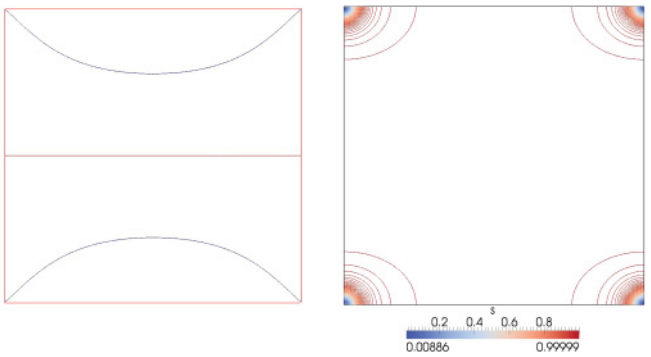

(a) Defects of the optimal R2-solution are close to but not exactly at the four corners.

(b) Contour lines of the order parameter of the optimal R2-solution.

FIG. 4. (Color online) (a) The two curved (blue) lines are where $Q_{11} = 0$, and the straight (red) lines (including the domain boundary) are where $Q_{12} = 0$. The defects are at the intersections of the two kinds of curves. (b) The contour lines from near the corners to the center correspond to increasing values of s with a step size of $\triangle s = 0.01$. The blank region in the center has s values in $[0.99,1]$. In both figures, the domain is the reference domain with width 1 (dimensionless). Parameters: $\varepsilon = 0.02$, mesh size $N = 256$, and $a_r = 1$.

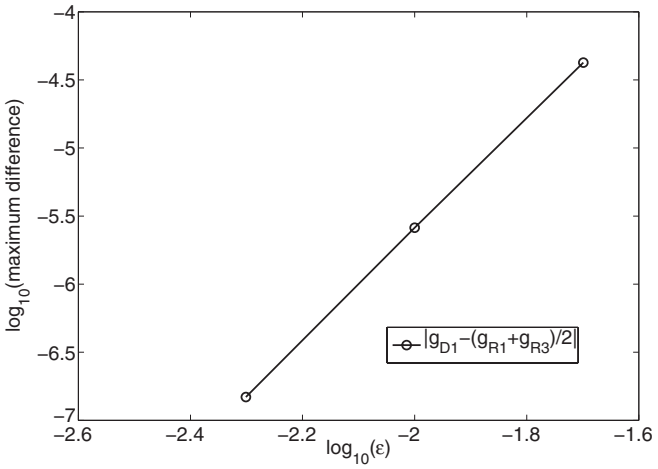

FIG. 5. Plot of $Y := \log_{10}|\boldsymbol{g}_{D1} - (\boldsymbol{g}_{R1} + \boldsymbol{g}_{R3})/2|$ vs $X := \log_{10}\varepsilon$. The fitted equation is $Y = 2.56 + 4.08X$. Parameters: mesh size $N = 256$ and $a_r = 1$.

boundary condition prescribes the optimal interpolation between $s = 0$ and $s = 1$ on the edges, i.e., the interpolation with the minimum associated energy cost. The optimal boundary conditions depend on ε and numerical results show that for each $\varepsilon > 0$, there are six optimal Dirichlet boundary conditions: $\boldsymbol{g}_{D1}, \boldsymbol{g}_{D2}, \boldsymbol{g}_{R1}, \boldsymbol{g}_{R2}, \boldsymbol{g}_{R3}, \boldsymbol{g}_{R4}$ with $\boldsymbol{g}_{D1} = \boldsymbol{g}_{D2}$, $\boldsymbol{g}_{R1} = \boldsymbol{g}_{R2}$, and $\boldsymbol{g}_{R3} = \boldsymbol{g}_{R4}$. However, $\boldsymbol{g}_{D1} \neq \boldsymbol{g}_{R1} \neq \boldsymbol{g}_{R3}$. On the one hand, we find that $\boldsymbol{g}_{D1}$ is very close to the average $(\boldsymbol{g}_{R1} + \boldsymbol{g}_{R3})/2$ and their maximum difference is proportional to ε^4, as shown in Fig. 5. On the other hand, the maximum differences $|\boldsymbol{g}_{D1} - \boldsymbol{g}_{R1}|$ and $|\boldsymbol{g}_{R1} - \boldsymbol{g}_{R3}|$ are proportional to ε^2, as shown in Fig. 6. Therefore, the differences between the optimal boundary conditions tend to zero as ε tends to zero. As mentioned before, in real physical setups, the dimensionless parameter ε is of the order of 10^{-5}, thus we expect that the differences between these optimal boundary conditions are negligible.

In the following sections, we fix the Dirichlet boundary condition to be $\boldsymbol{g} = \boldsymbol{g}_{D1} = \boldsymbol{g}_{D2}$, which is the optimal boundary

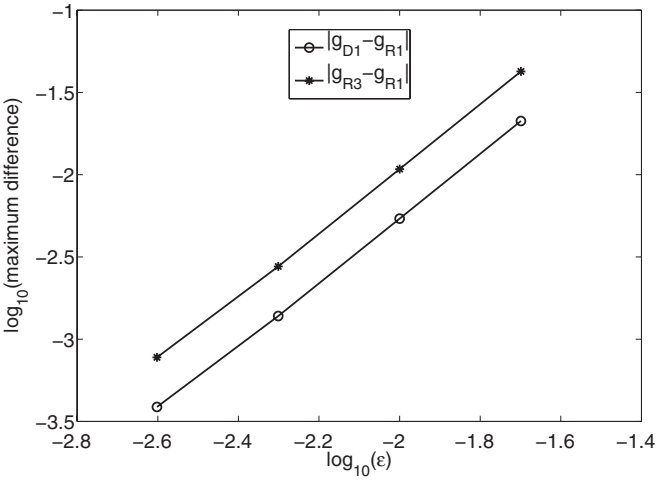

FIG. 6. Plot of $Y_1 := \log_{10}|\boldsymbol{g}_{D1} - \boldsymbol{g}_{R1}|$ and $Y_2 := \log_{10}|\boldsymbol{g}_{R3} - \boldsymbol{g}_{R1}|$ vs $X := \log_{10}\varepsilon$. The fitted equations are $Y_1 = 1.59 + 1.93X$ and $Y_2 = 1.90 + 1.93X$. Parameters: mesh size $N = 256$ and $a_r = 1$.

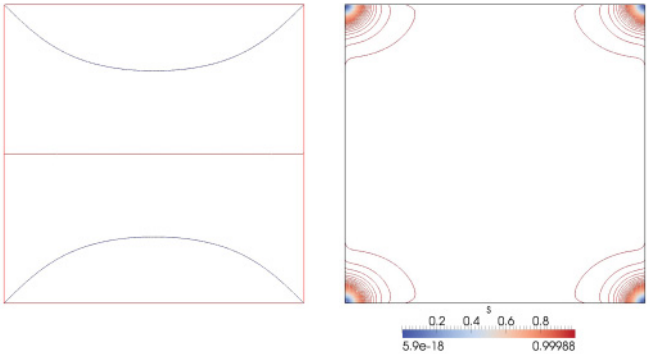

(a) Defects of the strong anchoring R2-solution are exactly at the four corners.

(b) Contour lines of the order parameter of the strong anchoring R2-solution.

FIG. 7. (Color online) (a) The two curved (blue) lines are where $Q_{11} = 0$, and the straight (red) lines (including the domain boundary) are where $Q_{12} = 0$. The defects are at the intersections of the two kinds of curves. (b) The contour lines from near the corners to the center correspond to increasing values of s with a step size of $\triangle s = 0.01$. The blank region in the center has s values in $[0.99, 1]$. In both figures, the domain is the reference domain with width 1 (dimensionless). Parameters: $\varepsilon = 0.02$, mesh size $N = 256$, and $a_r = 1$.

condition for the diagonal solutions, and use this to define an appropriate surface energy in the next section.

Since we fix the Dirichlet boundary condition $\boldsymbol{g}$ to be the optimal boundary condition of the diagonal solutions, the strong anchoring diagonal solutions are the same as the optimal diagonal solutions. However, the strong anchoring rotated solutions are different from the optimal rotated solutions. Figure 7 shows the defect locations and the order parameter contour lines for a strong anchoring R2 solution. We can see in Fig. 7(a) that unlike the optimal R2 solution, the defects of the strong anchoring R2 solution are located exactly at the four corners of the square domain. The order parameter contour lines are displayed in Fig. 7(b) and they are more skewed too.

IV. WEAK ANCHORING

In this section, we study the weak anchoring situation and replace the Dirichlet boundary condition with the surface anchoring energy (21). The total dimensionless energy is given by

$$\mathcal{E}[\boldsymbol{Q}] = \int_\Omega |\nabla Q_{11}|^2 + |\nabla Q_{12}|^2 + \frac{1}{\varepsilon^2}\left(Q_{11}^2 + Q_{12}^2 - 1\right)^2 dA + \int_{\partial\Omega} W|(Q_{11}, Q_{12}) - \boldsymbol{g}|^2 da, \tag{47}$$

where $\boldsymbol{g} = \boldsymbol{g}_{D1}$ is the Dirichlet boundary condition for the strong anchoring problem studied in Sec. III. This Dirichlet boundary condition depends on the choice of ε, as explained in the previous section. The admissible space for (Q_{11}, Q_{12}) is simply the Sobolev space $H^1(\Omega, \mathbb{R}^2)$.

By standard methods in the calculus of variations, local energy minimizers of (47) satisfy the following integral

equations:

$$0 = \int_\Omega \nabla Q_{11}\nabla v_{11} + \frac{2}{\varepsilon^2}\left(Q_{11}^2 + Q_{12}^2 - 1\right)Q_{11}v_{11}dA + \int_{\partial\Omega} W(Q_{11} - g_1)v_{11}da \quad \forall\, v_{11} \in H^1(\Omega), \tag{48}$$

$$0 = \int_\Omega \nabla Q_{12}\nabla v_{12} + \frac{2}{\varepsilon^2}\left(Q_{11}^2 + Q_{12}^2 - 1\right)Q_{12}v_{12}dA + \int_{\partial\Omega} W(Q_{12} - g_2)v_{12}da \quad \forall\, v_{12} \in H^1(\Omega), \tag{49}$$

where $(g_1, g_2) = \boldsymbol{g}$. Again we discretize these equations and solve using finite-element methods; the details can be found in the Appendix.

In Fig. 8, we display the defect locations and the order parameter contour lines for the weak anchoring D1 solution. Figure 8(a) shows that Q_{12} is always nonzero and therefore there is no defect for the weak anchoring D1 solution. Figure 8(b) shows that unlike the strong anchoring D1 solutions, the order parameter contour lines of the weak anchoring D1 solution are no longer circular. However, they are still symmetric about the center of the domain. Figure 9 shows the defect locations and the order parameter contour lines for the weak anchoring R2 solution. Figure 9(a) shows that the zero curves of Q_{11} and Q_{12} do not intersect, thus there is no defect for the weak anchoring R2 solution. The order parameter contour lines in Fig. 9(b) of the weak anchoring R2 solution look very similar to those of the weak anchoring D1 solution in Fig. 8(b). However, unlike the contour lines in Fig. 8(b), which are symmetric about the center of the square domain, the contour lines in Fig. 9(b) are symmetric about the horizontal center line $y = 0.5$. In both cases, the order parameter has a strictly positive minimum. We find that this minimum value approaches zero as we increase the dimensionless anchoring strength W. As mentioned at the end of Sec. II, in a real physical setup, the dimensionless anchoring strength W is of the order of 10^4, and we expect the

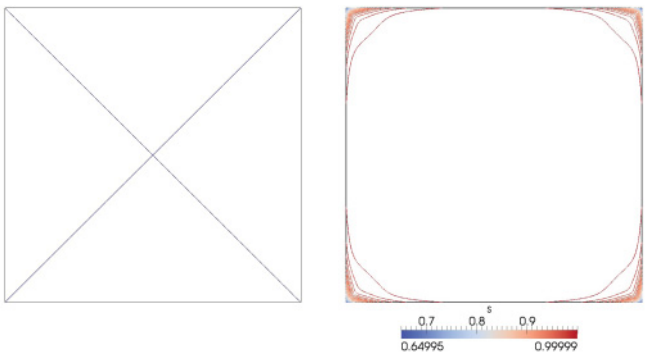

(a) No defect for the weak anchoring D1-solution.

(b) Contour lines of the order parameter of the weak anchoring D1-solution.

FIG. 8. (Color online) (a) The two diagonal (blue) curves are where $Q_{11} = 0$. There are no locations where $Q_{12} = 0$, thus there are no defects. (b) The contour lines from near the corners to the center correspond to increasing values of s with a step size of $\triangle s = 0.01$. The blank region in the center has s values in [0.99,1]. In both figures, the domain is the reference domain with width 1 (dimensionless). Parameters: $\varepsilon = 0.02$, mesh size $N = 256$, and $a_r = 1$.

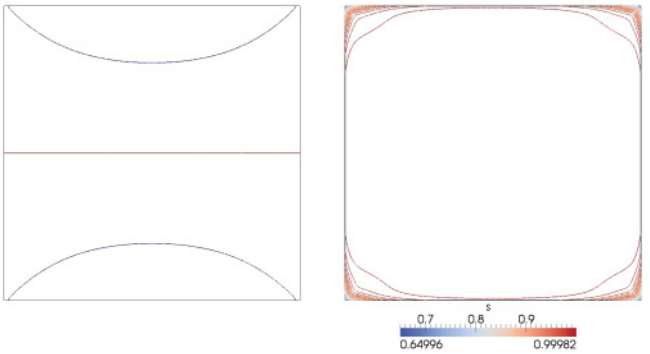

(a) No defect for the weak anchoring R2-solution.

(b) Contour lines of the order parameter of the weak anchoring R2-solution.

FIG. 9. (Color online) (a) The two curved (blue) lines are where $Q_{11} = 0$, and the center straight (red) line is where $Q_{12} = 0$. Since these two kinds of curves do not intersect, there are no defects. (b) The contour lines from near the corners to the center correspond to increasing values of s with a step size of $\triangle s = 0.01$. The blank region in the center has s values in [0.99,1]. In both figures, the domain is the reference domain with width 1 (dimensionless). Parameters: $\varepsilon = 0.02$, mesh size $N = 256$, and $a_r = 1$.

minimum value of the order parameter of the weak anchoring solutions to be much closer to zero. The numerical results show that the order parameters are less than unity for all $W > 0$, yielding physically realistic results.

For a fixed anchoring strength $W > 0$, there exist multiple weak anchoring solutions. To see how these solutions vary with the anchoring strength, we trace the solution branches using pseudo-arc-length continuation [27]. The resulting bifurcation diagram for $\varepsilon = 0.02$ and $a_r = 1$ is shown in Fig. 10, where the x axis is the anchoring strength W and the y axis is the average of the angles over half of the top edge, $\{(x,1) : 0 < x < \frac{1}{2}\}$ (with unit π). We find that this average is suitable for distinguishing between the different solution profiles and is a better measure than the average over the whole top edge. For example, in the case of the R3 and R4 solutions, the directors at the top edge are symmetric about the midpoint of the top edge, and thus the average over the entire top edge is around $\pi/2$ in both cases. By plotting typical director profiles from each solution branch, we find that for large enough $W > 0$, the six solutions from top to bottom are R4, D2, R2, R1, D1, and R3, respectively (see Fig. 1 to recall the corresponding director profiles). We note that the diagonal solutions, D1 and D2, exist for all $W \geqslant 0$, while the rotated solutions, R1, R2, R3, and R4, only exist for $W \geqslant W_c \approx 2.7$. Further, the R1 and R2 solutions are in the same branch, while the R3 and R4 solutions are in the same branch. We find that at $W = 0$, the D1 solutions degenerate to the constant solution $(Q_{11}, Q_{12}) \equiv (0,1)$ (which corresponds to $\theta \equiv \pi/4$), while the D2 solutions degenerate to the constant solution $(Q_{11}, Q_{12}) \equiv (0, -1)$ (which corresponds to $\theta \equiv 3\pi/4$). At $W = W_c$, although the director profiles show that R1 and R2 solutions degenerate to a solution with $\theta \equiv \pi/2$, and the R3 and R4 solutions degenerate to a solution with $\theta \equiv 0$, these degenerate solutions do not have constant (Q_{11}, Q_{12}) values across the domain. Since $\boldsymbol{g}$ is not constant on $\partial\Omega$,

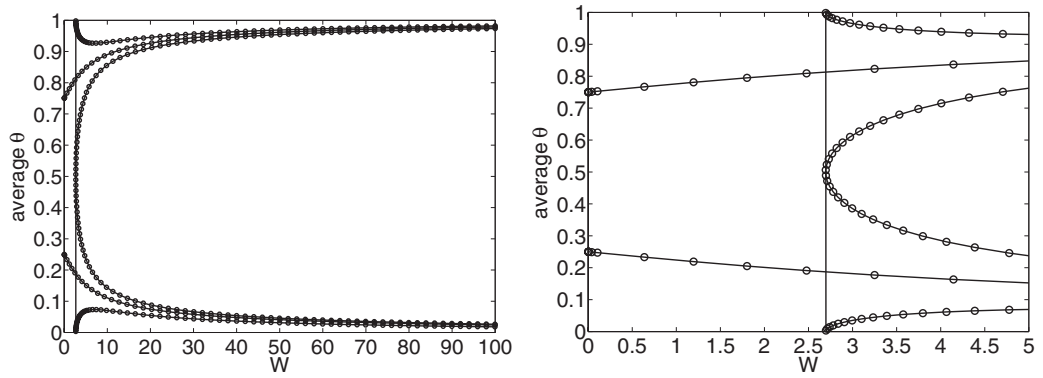

(a) The whole picture.

(b) Zoom-in near the critical anchoring strength.

FIG. 10. The bifurcation diagram. Parameters: $\varepsilon = 0.02$, mesh size $N = 32$, and $a_r = 1$.

constant-valued solutions cannot satisfy Eqs. (48) and (49) at $W = W_c > 0$. We have produced videos that demonstrate how the solutions change as we move along different branches in the bifurcation diagram. See Supplemental Material [28] for the evolution of these solutions along the D1, D2, R2-R1, and R4-R3 branches.

We have studied the stability of the distinct equilibria and have found that all six equilibria in Fig. 10 are stable. The details of the stability analysis can be found in the Appendix. As $W \to \infty$, the weak anchoring solutions converge to their strong anchoring counterparts in $H^1(\Omega)$, as shown in Fig. 11. This is a prerequisite for any viable surface anchoring energy.

Figure 12 illustrates how the critical anchoring strength W_c varies with the parameter ε. Recall that ε is related to the material parameters by (28). We can see that W_c decreases linearly as $\varepsilon \to 0$. The fitted equation is $W_c(\varepsilon) = 2.54 + 10.30\varepsilon$, which suggests that W_c might remain a positive constant in the limit $\varepsilon \to 0$. That is, in the limit $\varepsilon \to 0$, the rotated solutions do not exist unless the anchoring strength is sufficiently strong.

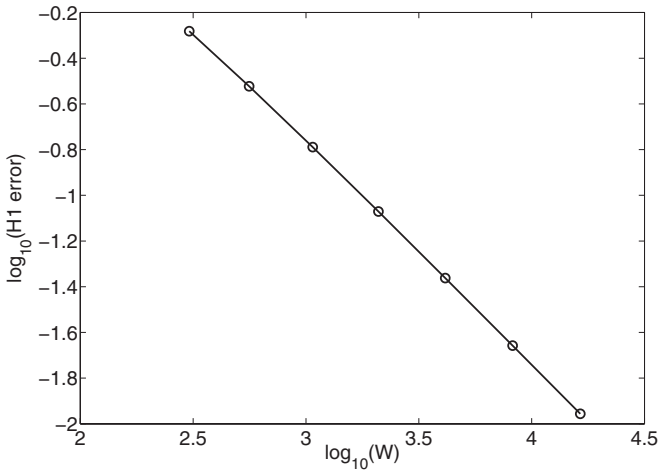

FIG. 11. Plot of $Y := \log_{10} \|\boldsymbol{u}_W - \boldsymbol{u}\|_1$ vs $X := \log_{10} W$, where $\boldsymbol{u}_W$ is the weak anchoring D1 solution at anchoring strength W, and $\boldsymbol{u}$ is the strong anchoring D1 solution (see Sec. III). The fitted equation is $Y = 2.14 - 0.97X$. Parameters: $\varepsilon = 0.02$, mesh size $N = 32$, and $a_r = 1$.

This is consistent with the global energy-minimizing property of the diagonal solutions.

V. SWITCHING UNDER ELECTRIC FIELD

In this section, we model the switching mechanisms between different stable states under the action of an external electric field, in the weak anchoring setup.

By gradient flow analysis, the dynamic equations associated with the dimensionless free energy in (31) are given by [24]

$$\frac{\partial Q_{11}}{\partial t} = \triangle Q_{11} - \frac{2}{\varepsilon^2}\left(Q_{11}^2 + Q_{12}^2 - 1\right)Q_{11} - \frac{1}{2}\mathrm{sgn}(C_0)E^2\cos(2\theta_E) \quad \text{in } \Omega, \tag{50}$$

$$\frac{\partial Q_{12}}{\partial t} = \triangle Q_{12} - \frac{2}{\varepsilon^2}\left(Q_{11}^2 + Q_{12}^2 - 1\right)Q_{12} - \frac{1}{2}\mathrm{sgn}(C_0)E^2\sin(2\theta_E) \quad \text{in } \Omega, \tag{51}$$

$$\frac{\partial Q_{11}}{\partial t} = -\frac{\partial Q_{11}}{\partial \boldsymbol{\nu}} - W(Q_{11} - g_1) \quad \text{on } \partial\Omega, \tag{52}$$

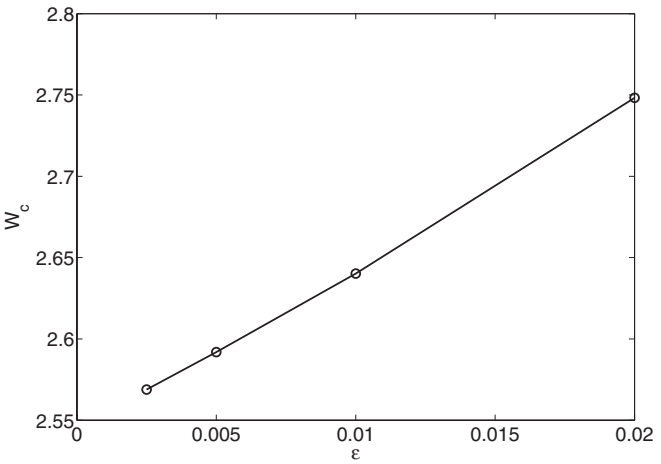

FIG. 12. Critical anchoring strength W_c vs ε. The fitted equation is $W_c(\varepsilon) = 2.54 + 10.30\varepsilon$. Parameters: mesh size $N = 256$ and $a_r = 1$.

$$\frac{\partial Q_{12}}{\partial t} = -\frac{\partial Q_{12}}{\partial \boldsymbol{\nu}} - W(Q_{12} - g_2) \quad \text{on } \partial\Omega, \tag{53}$$

where $(g_1, g_2) = \boldsymbol{g}_{\mathrm{D1}}$, as stated in Sec. IV. Here, t is dimensionless and can be related to the physical time $\tilde{t}$ by

$$t = \frac{L_{el}}{\gamma L^2}\tilde{t}, \tag{54}$$

and γ is a viscosity coefficient with units $\mathrm{N\,s\,m^{-1}}$ [29]. We use the finite difference method [30] to simulate the dynamics under an electric field. We discretize the rectangular domain using a uniform $N \times (N \cdot a_r)$ mesh, approximate the Laplace operator $\triangle$ using a five-point stencil, approximate $\partial/\partial \boldsymbol{\nu}$ using backward difference, and approximate $\partial/\partial t$ using forward difference [30].

A typical switching process consists of two steps. In the first step, we switch on the electric field and wait for the system to reach equilibrium. In the second step, we switch off the electric field and wait for the system to reach equilibrium again. In the following numerical simulation, the system is regarded to be in the equilibrium state when the l^2 difference [31] between the solutions of adjacent time steps is less than $\tau = 10^{-3}$.

We first investigate the situation of constant anchoring strength W on $\partial\Omega$. We find that the rotated-to-diagonal switching can be easily achieved by applying uniform electric fields in the diagonal directions. The diagonal-to-rotated switching is more difficult to accomplish. We have achieved switching from D1 to R2 solutions using the following patched electric fields on a square domain:

$$\boldsymbol{E} = \begin{cases} 10[\cos(\pi/4), \sin(\pi/4)], & y \in [0, 1/8], \\ 10[\cos(\pi/2), \sin(\pi/2)], & y \in [1/8, 7/8], \\ 10[\cos(3\pi/4), \sin(3\pi/4)], & y \in (7/8, 1], \end{cases}$$

and by using the following linear electric fields on a rectangular domain with $a_r = 2$:

$$\boldsymbol{E} = 10\frac{y}{a_r}[\cos(3\pi/4), \sin(3\pi/4)]. \tag{55}$$

However, these nonuniform electric fields are not easy to implement in practice because the physical domain can be as small as 80 μm [8].

Using a nonuniform anchoring strength on the boundary can also facilitate diagonal-to-rotated switching, and this can be much easier to physically implement than nonuniform electric fields. One possible framework is to make the anchoring strength on the top edge much weaker than that on the rest of the domain boundary. For example,

$$W = \begin{cases} 10 & \text{on } y = a_r, \\ 100 & \text{otherwise.} \end{cases} \tag{56}$$

With the anchoring strength given by (56), the R2 to D1 switching can be achieved using

$$\boldsymbol{E} = 10[\cos(\pi/4), \sin(\pi/4)],$$

and the D1 to R2 switching can be achieved using

$$\boldsymbol{E} = 10[\cos(3\pi/4), \sin(3\pi/4)]. \tag{57}$$

We can qualitatively understand this switching phenomenon by recalling the D1 and R2 alignment profiles from Fig. 1. The D1 solutions correspond to the boundary conditions $\theta(x,0) = \theta(x,a_r) = 0$ and $\theta(0,y) = \theta(1,y) = \frac{\pi}{2}$, whereas the R2 solutions correspond to the boundary conditions $\theta(x,0) = 0$, $\theta(x,a_r) = \pi$, and $\theta(0,y) = \theta(1,y) = \frac{\pi}{2}$. Hence, the two solution profiles are distinguished by their alignment profile on the top edge. In (56), we have made the anchoring strength on the top edge ten times smaller than that on the remaining three edges so that the nonequilibrium configurations in the presence of the uniform diagonal electric field (57) can break the anchoring on the top edge and then relax into the R2 state once the electric field is removed.

Figure 13 demonstrates the switching mechanism from R2 to D1, while Fig. 14 shows the switching mechanism from D1 to R2. Note that for the same electric field strength, the switching from D1 to R2 is slightly slower than the switching from R2 to D1. This is possibly because the D1 solution has lower energy than the R2 solution, and there is a higher energy barrier to be overcome before the system can get out of the D1 equilibrium.

We find that during the switching process, the order parameter s does not change much in the domain except for at the top edge, where the order parameter first decreases until the directors are largely vertical, and then the order parameter increases again until the completion of the switching process. We believe that the switching is induced by a competition between the applied electric field and the anchoring on the top edge. Since the anchoring on the top edge is relatively weak, the directors prefer to align with the externally applied electric field for large enough $|\boldsymbol{E}|$, during the nonequilibrium dynamics. This is enough to break the anchoring on the top edge and, once the field has been removed, the directors relax into the other competing static equilibrium state. We have produced videos showing how the order parameter and director profile change during the switching process. See Supplemental Material [28] for the switching from D1 to R2 with the electric field on and off and the switching from R2 to D1 with the electric field on and off, respectively.

VI. CONCLUSION AND DISCUSSION

We have mathematically modeled and analyzed a planar bistable liquid crystal device with tangent boundary conditions, as has been reported in [8]. We have modeled the static equilibria and the switching mechanisms in this device within the Landau-de Gennes theory for nematic liquid crystals. Of prime importance in our analysis is the dimensionless parameter $\tilde{\varepsilon}$, defined in terms of the material parameters ε, L_{el} and the device width L. This parameter is typically very small for macroscopic domains and enforces the constraint $s = s_0$ almost everywhere in the domain, for stable equilibria, where s_0 is the preferred bulk order parameter as given by (14). Further, this parameter dictates the effective defect core size, which is proportional to $\tilde{\varepsilon}L$ where L is the width of the square well. For a fixed temperature, the quantity $\tilde{\varepsilon}L$ only depends on material parameters L_{el} and c, and does not depend on the width L of the square well. For larger values of $\tilde{\varepsilon}$, we will not obtain well-ordered optically contrasting textures and the singular regions near the vertices will spread out into the domain interior resulting in undesirable optical properties.

We have introduced the concept of an optimal Dirichlet boundary condition which, in turn, depends on the material

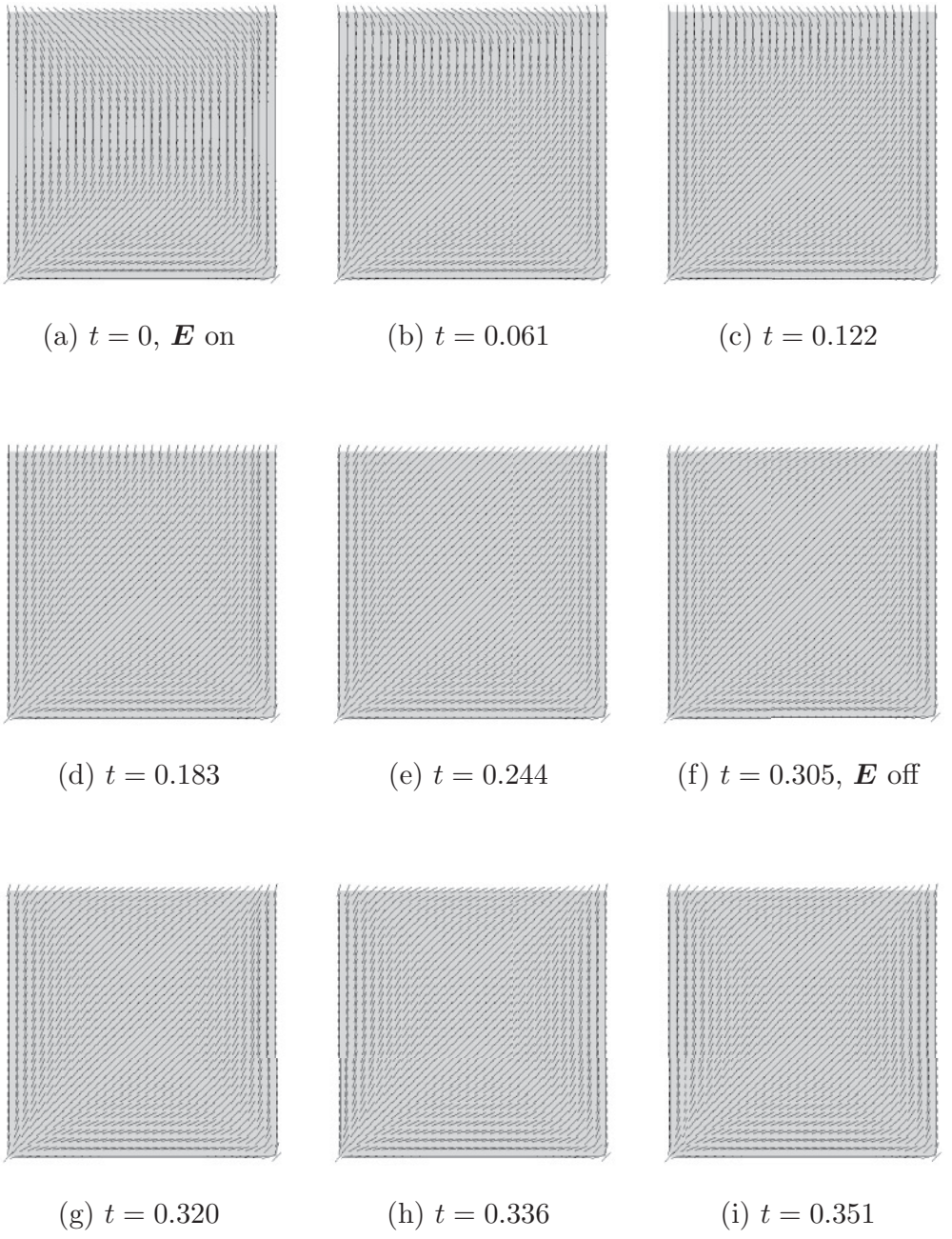

(a) $t = 0$, $\boldsymbol{E}$ on (b) $t = 0.061$ (c) $t = 0.122$

(d) $t = 0.183$ (e) $t = 0.244$ (f) $t = 0.305$, $\boldsymbol{E}$ off

(g) $t = 0.320$ (h) $t = 0.336$ (i) $t = 0.351$

FIG. 13. The switching from R2 to D1. Parameters: $\varepsilon = 0.02$, $\boldsymbol{E} = 10[\cos(\pi/4), \sin(\pi/4)]$, mesh size $N = 32$, time step $\triangle t = 1/N^3$, $\tau = 10^{-3}$, and W is given by (56).

parameters ε, L_{el} and the device width L through the dimensionless parameter $\tilde{\varepsilon}$. These optimal boundary conditions have been numerically computed and they can be used to systematically investigate the relationships between material properties, device geometry, and equilibrium and nonequilibrium properties. We have numerically studied defect locations and defect profiles in the strong anchoring case and our numerical simulations suggest slightly different defect profiles for the diagonal and rotated solutions. In the weak anchoring case, we have proposed a surface anchoring energy in terms of an anchoring coefficient W and the optimal Dirichlet boundary condition, i.e., the surface anchoring energy incorporates coupling effects between the surface anchoring strength W and bulk parameters such as ε and L_{el}. We have studied the multiplicity and the stability of static equilibria as a function of the anchoring strength W and have found that the device is bistable or multistable for $W \geqslant W_c > 0$, where the critical anchoring strength W_c depends on material parameters through the dimensionless variable $\tilde{\varepsilon}$. For $W \geqslant W_c$, we have found six competing static equilibria, which mimic the experimentally observed diagonal and rotated profiles in [8]. We have investigated the dependence of W_c on the parameter $\tilde{\varepsilon}$, and numerical investigations indicate a linear scaling. It is interesting that the rotated solutions only exist for $W \geqslant W_c$, whereas the diagonal solutions seem to exist for all $W \geqslant 0$. We conjecture that the normal derivative of the rotated solutions

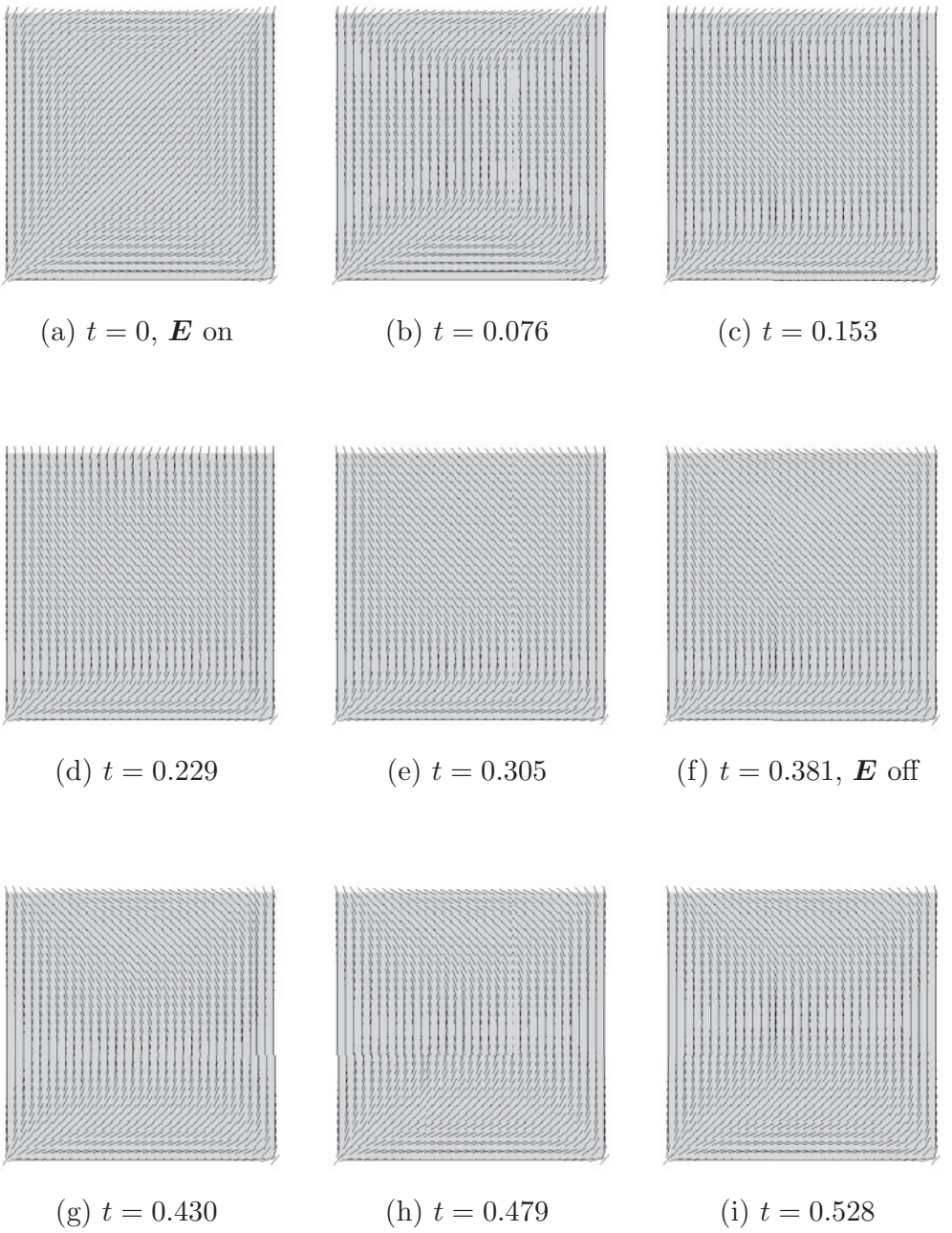

(a) $t = 0$, $\boldsymbol{E}$ on (b) $t = 0.076$ (c) $t = 0.153$

(d) $t = 0.229$ (e) $t = 0.305$ (f) $t = 0.381$, $\boldsymbol{E}$ off

(g) $t = 0.430$ (h) $t = 0.479$ (i) $t = 0.528$

FIG. 14. The switching from D1 to R2. Parameters: $\varepsilon = 0.02$, $\boldsymbol{E} = 10[\cos(3\pi/4), \sin(3\pi/4)]$, mesh size $N = 32$, time step $\triangle t = 1/N^3$, $\tau = 10^{-3}$, and W is given by (56).

does not tend to zero uniformly as the anchoring coefficient W tends to zero, and hence W must be sufficiently large to balance the normal derivative, $\frac{\partial \boldsymbol{Q}}{\partial \boldsymbol{\nu}}$, in (52) and (53). Further, we do not observe any isotropic points in the weak anchoring case since it is energetically preferable to violate the tangent boundary conditions near the vertices and escape from the energetically expensive isotropic phase (recall that small values of $\tilde{\varepsilon}$ are accompanied by a heavy energetic penalty for deviations away from $s = s_0$ in the domain).

We have proposed a simple dynamic model for the switching characteristics of this device that is based on dielectric effects and the concept of variable anchoring strength across the domain boundary. The anchoring is weaker on the subset of the boundary, which induces the transition between two stable static equilibria, and the switching is mediated by the competition between the external electric field and anchoring effects. We have studied the switching between the D1 and R2 solutions and the same concepts can be applied to study switching between different pairs of static equilibria. This is the simplest model for the switching characteristics and a larger class of physical phenomena, e.g., flexoelectricity, backflow effects, coupling between fluid velocity and nematic order, needs to be included for a complete understanding.

The results of this paper can be extrapolated to three dimensions (3D) as follows. In 3D, the $\boldsymbol{Q}$ tensor is a 3×3 symmetric traceless matrix with five degrees of freedom. In the

uniaxial case, the $\boldsymbol{Q}$ tensor only has three degrees of freedom and it can be written in the simpler form as $\boldsymbol{Q} = s(\boldsymbol{n} \otimes \boldsymbol{n} - \frac{1}{3}I)$, where s is the order parameter and $\boldsymbol{n} = (n_1,n_2,n_3)^T \in S^2$ is the director. We define $\boldsymbol{q} = \sqrt{s}\boldsymbol{n}$. Then we have $\boldsymbol{Q} = \boldsymbol{q}\boldsymbol{q}^T - \frac{1}{3}\boldsymbol{q}^T\boldsymbol{q}$ and the Landau-de Gennes energy can be written as a functional of $\boldsymbol{q}$. The 3D physical domain is a box. In the strong anchoring case, we impose a Dirichlet boundary condition $\boldsymbol{q} = \boldsymbol{q}_0$ on the six faces of the box. The boundary condition $\boldsymbol{q}_0$ should be consistent with the in-plane anchoring. Specifically, for the faces in the xy plane, in-plane anchoring requires that $n_3 = 0$, which in turn implies that $q_3 = 0$. Similarly, for the faces in the yz plane, we have $q_1 = 0$, and for the two faces in the xz plane, we have $q_2 = 0$. One can similarly compute the optimal boundary conditions, define the corresponding strong anchoring and weak anchoring problems, and then model the switching under an external electric field. One can also relax the uniaxiality assumption and use the full $\boldsymbol{Q}$ tensor, with five degrees of freedom, allowing for biaxiality. The paper [32] describes a finite-element method for this approach, and uses it to study a π cell and a hybrid cell. Similar techniques may also be applied to 3D liquid crystal wells.

ACKNOWLEDGMENTS

We thank Professor Nigel Mottram and Dr. Peter Howell for helpful discussions. This publication was based on work supported in part by Award No KUK-C1-013-04, made by King Abdullah University of Science and Technology (KAUST). A.M.'s research is also supported by an EPSRC Career Acceleration Fellowship No. EP/J001686/1. The research leading to these results has received funding from the European Research Council under the European Community's Seventh Framework Programme (FP7/2007-2013)/ ERC Grant Agreement No. 239870. R.E. would also like to thank Somerville College, University of Oxford, support from a Fulford Junior Research Fellowship; Brasenose College, University of Oxford, support from a Nicholas Kurti Junior Fellowship; the Royal Society support from a University Research Fellowship, and the Leverhulme Trust for support from a Philip Leverhulme Prize.

APPENDIX: NUMERICAL METHODS

In this section, we give some technical details for the numerical methods. We have solved the integral equations (41) and (42), (44) and (45), and (48) and (49) with finite-element methods. Recall that (41) and (42) correspond to the strong anchoring solutions, (44) and (45) correspond to the optimal solutions, and (48) and (49) correspond to the weak anchoring solutions. We partition the domain $\Omega = [0,1] \times [0,a_r]$ into a uniform $N \times (a_r \cdot N)$ triangular mesh and approximate $H^1(\Omega)$ using piecewise linear finite elements [26]. After the discretization, the integral equations become a nonlinear system of equations for the degrees of freedom (Q_{11},Q_{12}), and are solved using Newton's method [30]. Newton's method strongly depends on the initial condition, and to obtain the six different solutions D1, D2, R1, R2, R3, and R4, we simply use six different initial conditions.

For a given Dirichlet boundary condition $\boldsymbol{g}$, we construct the initial conditions for the strong anchoring problem as follows,

TABLE II. The six different initial conditions for Newton's method.

Solution	$x = 0$	$x = 1$	$y = 0$	$y = a_r$
D1	$\pi/2$	$\pi/2$	0	0
D2	$\pi/2$	$\pi/2$	π	π
R1	$\pi/2$	$\pi/2$	π	0
R2	$\pi/2$	$\pi/2$	0	π
R3	$3\pi/2$	$\pi/2$	π	π
R4	$\pi/2$	$3\pi/2$	π	π

taking the D1 solution as an example. We first solve the Laplace equation $\triangle\theta = 0$ on the uniform mesh using the finite difference method with the discontinuous boundary condition $\theta(0,y) = \theta(1,y) = \frac{\pi}{2}$ and $\theta(x,0) = \theta(x,a_r) = 0$. Next, we construct $(Q_{11},Q_{12}) = s(\cos 2\theta, \sin 2\theta)$, where $s = 1$ at the interior nodes and $s = |\boldsymbol{g}|$ at the boundary nodes. Then we use the resulting (Q_{11},Q_{12}) as the initial condition for the strong anchoring D1 solution. In Table II, we enumerate the boundary conditions for all six types of initial conditions. For a fixed $d > 0$, we define the vector field $\boldsymbol{g}_d$ to be

$$\boldsymbol{g}_d = \begin{cases} [T_d(x),0] & \text{on } y = 0 \text{ and } y = a_r, \\ \left[-T_{\frac{d}{a_r}}\left(\frac{y}{a_r}\right),0\right] & \text{on } x = 0 \text{ and } x = 1, \end{cases} \tag{A1}$$

where the trapezoidal shape function $T_d : [0,1] \to \mathbb{R}$ is given by

$$T_d(t) = \begin{cases} t/d, & 0 \leqslant t \leqslant d, \\ 1, & d \leqslant t \leqslant 1-d, \\ (1-t)/d, & 1-d \leqslant t \leqslant 1. \end{cases} \tag{A2}$$

The parameter d is in the range $d \in (0,0.5]$. To obtain the optimal solutions, we use the strong anchoring solutions for $\boldsymbol{g} = \boldsymbol{g}_{3\varepsilon}$ as the initial conditions. For the weak anchoring solutions with large anchoring strength $W > 0$, we use the strong anchoring solutions as initial conditions for Newton's method. Then we use numerical continuation to obtain solutions for smaller W.

Once we obtain the solutions with Newton's method, we compute their energies by numerical integration techniques. In this paper, all finite-element simulations and numerical integrations have been performed using the open-source package FEniCS [33].

Tables III–V show the numerical errors, energies, and their orders of convergence for some typical optimal solutions, strong anchoring solutions, and weak anchoring solutions, respectively. We can see that in all cases, we have order 2 convergence for the L^2 errors and the total energies, and order 1 convergence for the H^1 errors. We also observe that in all cases, the diagonal solutions have lower energies than the rotated solutions.

Next, we give details for the stability analysis in the weak anchoring case. By gradient flow analysis [24], solutions of the weak anchoring problem satisfy the following dynamic equations:

$$\frac{\partial Q_{11}}{\partial t} = \triangle Q_{11} - \frac{2}{\varepsilon^2}\left(Q_{11}^2 + Q_{12}^2 - 1\right)Q_{11} \quad \text{in } \Omega, \tag{A3}$$

$$\frac{\partial Q_{12}}{\partial t} = \triangle Q_{12} - \frac{2}{\varepsilon^2}\left(Q_{11}^2 + Q_{12}^2 - 1\right)Q_{12} \quad \text{in } \Omega, \tag{A4}$$

TABLE III. Numerical errors, energies, and their orders of convergence for the optimal solutions. Parameters: $\varepsilon = 0.02$ and $a_r = 1$.

The optimal D1 solution						
N	L^2 err	order	H^1 err	order	Energy	order
16	3.71×10^{-2}		2.80		90.803	
32	1.15×10^{-2}	1.68	1.65	0.76	81.337	1.74
64	3.31×10^{-3}	1.80	0.874	0.92	78.500	1.89
128	8.76×10^{-4}	1.92	0.443	0.98	77.734	1.96
256	2.23×10^{-4}	1.97	0.222	0.99	77.538	1.99
The optimal R2 solution						
16	3.99×10^{-2}		2.85		99.878	
32	1.19×10^{-2}	1.74	1.67	0.77	90.056	1.76
64	3.39×10^{-3}	1.81	0.882	0.92	87.153	1.89
128	8.93×10^{-4}	1.92	0.447	0.98	86.373	1.97
256	2.27×10^{-4}	1.98	0.224	0.99	86.173	1.99

$$\frac{\partial Q_{11}}{\partial t} = -\frac{\partial Q_{11}}{\partial \boldsymbol{\nu}} - W(Q_{11} - g_1) \quad \text{on } \partial\Omega, \tag{A5}$$

$$\frac{\partial Q_{12}}{\partial t} = -\frac{\partial Q_{12}}{\partial \boldsymbol{\nu}} - W(Q_{12} - g_2) \quad \text{on } \partial\Omega. \tag{A6}$$

The corresponding weak formulation is the following:

$$\begin{aligned}\int_\Omega \frac{\partial Q_{11}}{\partial t} v_{11} dA + \int_{\partial\Omega} \frac{\partial Q_{11}}{\partial t} v_{11} da \\ = -\int_\Omega \nabla Q_{11} \nabla v_{11} + \frac{2}{\varepsilon^2}\left(Q_{11}^2 + Q_{12}^2 - 1\right) Q_{11} v_{11} dA \\ - \int_{\partial\Omega} W(Q_{11} - g_1) v_{11} da \quad \forall\, v_{11} \in H^1(\Omega),\end{aligned} \tag{A7}$$

$$\begin{aligned}\int_\Omega \frac{\partial Q_{12}}{\partial t} v_{12} dA + \int_{\partial\Omega} \frac{\partial Q_{12}}{\partial t} v_{12} da \\ = -\int_\Omega \nabla Q_{12} \nabla v_{12} + \frac{2}{\varepsilon^2}\left(Q_{12}^2 + Q_{12}^2 - 1\right) Q_{12} v_{12} dA \\ - \int_{\partial\Omega} W(Q_{12} - g_2) v_{12} da \quad \forall\, v_{12} \in H^1(\Omega).\end{aligned} \tag{A8}$$

TABLE IV. Numerical errors, energies, and their orders of convergence for the strong anchoring solutions. Parameters: $\varepsilon = 0.02$ and $a_r = 1$.

The rotated solution R2						
N	L^2 err	order	H^1 err	order	Energy	order
16	4.04×10^{-2}		2.85		99.896	
32	1.19×10^{-2}	1.77	1.67	0.77	90.056	1.76
64	3.38×10^{-3}	1.81	0.882	0.92	87.155	1.89
128	8.90×10^{-4}	1.92	0.447	0.98	86.375	1.97
256	2.26×10^{-4}	1.98	0.224	0.99	86.175	1.99
The rotated solution R3						
16	4.04×10^{-2}		2.85		99.896	
32	1.19×10^{-2}	1.77	1.67	0.77	90.056	1.76
64	3.38×10^{-3}	1.81	0.882	0.92	87.155	1.89
128	8.90×10^{-4}	1.92	0.447	0.98	86.375	1.97
256	2.26×10^{-4}	1.98	0.224	0.99	86.175	1.99

TABLE V. Numerical errors, energies, and their orders of convergence for the weak anchoring solutions. Parameters: $\varepsilon = 0.02$, $W = 50$, and $a_r = 1$.

The diagonal solution D1						
N	L^2 err	order	H^1 err	order	Energy	order
32	6.63×10^{-3}		1.08		64.448	
64	1.81×10^{-3}	1.88	0.581	0.90	62.928	1.98
128	4.64×10^{-4}	1.96	0.296	0.97	62.544	1.99
256	1.17×10^{-4}	1.98	0.149	0.99	62.446	1.99
The rotated solution R2						
N	L^2 err	order	H^1 err	order	Energy	order
32	7.25×10^{-3}		1.11		73.156	
64	1.93×10^{-3}	1.91	0.591	0.90	71.579	1.99
128	4.95×10^{-4}	1.97	0.302	0.97	71.181	1.99
256	1.25×10^{-4}	1.99	0.152	0.99	71.081	1.99

We discretize (A7) and (A8) using continuous piecewise linear finite elements on a uniform $N \times (a_r \cdot N)$ mesh, and discretize the time derivative $\partial/\partial t$ using forward difference. We denote the mesh width as $h = 1/N$ and the time-step size as $\triangle t$. We denote the finite-element space as V_h. Then the discretized version of (A7) and (A8) is

$$\begin{aligned}\int_\Omega \frac{Q_{11}^{(n+1)} - Q_{11}^{(n)}}{\triangle t} v_{11} dA + \int_{\partial\Omega} \frac{Q_{11}^{(n+1)} - Q_{11}^{(n)}}{\triangle t} v_{11} da \\ = -\int_\Omega \nabla Q_{11}^{(n)} \nabla v_{11} + \frac{2}{\varepsilon^2}\left[\left(Q_{11}^{(n)}\right)^2 + \left(Q_{12}^{(n)}\right)^2 - 1\right] Q_{11}^{(n)} v_{11} dA \\ - \int_{\partial\Omega} W(Q_{11}^{(n)} - g_1) v_{11} da \quad \forall\, v_{11} \in V_h,\end{aligned} \tag{A9}$$

$$\begin{aligned}\int_\Omega \frac{Q_{12}^{(n+1)} - Q_{12}^{(n)}}{\triangle t} v_{12} dA + \int_{\partial\Omega} \frac{Q_{12}^{(n+1)} - Q_{12}^{(n)}}{\triangle t} v_{12} da \\ = -\int_\Omega \nabla Q_{12}^{(n)} \nabla v_{12} + \frac{2}{\varepsilon^2}\left[\left(Q_{12}^{(n)}\right)^2 + \left(Q_{12}^{(n)}\right)^2 - 1\right] Q_{12}^{(n)} v_{12} dA \\ - \int_{\partial\Omega} W(Q_{12}^{(n)} - g_2) v_{12} da \quad \forall\, v_{12} \in V_h,\end{aligned} \tag{A10}$$

where the parenthesized superscripts mean time step. Let the degrees of freedom of (Q_{11}, Q_{12}) at time step n be $\boldsymbol{u}^{(n)}$. Since we use piecewise linear finite elements, (A9) and (A10) can be written as

$$\boldsymbol{M}(\boldsymbol{u}^{(n+1)} - \boldsymbol{u}^{(n)}) = \triangle t \boldsymbol{\phi}(\boldsymbol{u}^{(n)}), \tag{A11}$$

where $\boldsymbol{M}$ is a matrix and $\boldsymbol{\phi}$ is a nonlinear function. Denote $\boldsymbol{f} \triangleq I + \triangle t \boldsymbol{M}^{-1}\boldsymbol{\phi}$, then (A11) becomes

$$\boldsymbol{u}^{(n+1)} = \boldsymbol{f}(\boldsymbol{u}^{(n)}). \tag{A12}$$

The linear stability of an equilibrium solution $\boldsymbol{u}$ of the discrete map (A12) is then determined by $\nabla \boldsymbol{f}(\boldsymbol{u})$ [34]. It is easy to check that $\nabla \boldsymbol{f}(\boldsymbol{u}) = \boldsymbol{I} - \triangle t \boldsymbol{A}(\boldsymbol{u})$, where $\boldsymbol{A}(\boldsymbol{u}) = -\boldsymbol{M}^{-1}\nabla\boldsymbol{\phi}(\boldsymbol{u})$. In the limit $\triangle t \to 0$, the asymptotic linear stability of an equilibrium solution $\boldsymbol{u}$ is then simply determined by the positivity of the smallest eigenvalue λ_1 of the matrix $\boldsymbol{A}$, which can be computed using the ARPACK++ package [35].

[1] E. Lueder, *Liquid Crystal Displays: Addressing Schemes and Electro-optical Effects* (Wiley, West Sussex, UK, 2010).
[2] B. Bahadur, *Liquid Crystals: Applications and Uses* (World Scientific, Singapore, 1990), Vol. 1.
[3] P. G. de Gennes and J. Prost, *The Physics of Liquid Crystals* (Oxford University Press, New York, 1995).
[4] I. Dozov, M. Nobili, and G. Durand, Appl. Phys. Lett. **70**, 1179 (1997).
[5] S. Kitson and A. Geisow, Appl. Phys. Lett. **80**, 3635 (2002).
[6] A. Majumdar, C. J. P. Newton, J. M. Robbins, and M. Zyskin, Phys. Rev. E **75**, 051703 (2007).
[7] T. J. Spencer, C. M. Care, R. M. Amos, and J. C. Jones, Phys. Rev. E **82**, 021702 (2010).
[8] C. Tsakonas, A. J. Davidson, C. V. Brown, and N. J. Mottram, Appl. Phys. Lett. **90**, 111913 (2007).
[9] Y. Yi, M. Nakata, A. R. Martin, and N. A. Clark, Appl. Phys. Lett. **90**, 163510 (2007).
[10] Y. Yi, G. Lombardo, N. Ashby, R. Barberi, J. E. Maclennan, and N. A. Clark, Phys. Rev. E **79**, 041701 (2009).
[11] A. J. Davidson and N. J. Mottram, Phys. Rev. E **65**, 051710 (2002).
[12] F. C. Frank, Discuss. Faraday Soc. **25**, 19 (1958).
[13] A. Majumdar, Commun. Pure Appl. Anal. **11**, 1303 (2012).
[14] R. A. Adams and J. J. F. Fournier, *Sobolev Spaces* (Academic, New York, 1975), Vol. 65.
[15] A. Majumdar, J. Robbins, and M. Zyskin, J. Phys. A **37**, L573 (2004).
[16] P. A. Krutitskii, Q. Appl. Math. **66**, 177 (2008).
[17] A. Majumdar and A. Zarnescu, Arch. Ration. Mech. Anal. **196**, 227 (2010).
[18] A. Majumdar, Eur. J. Appl. Math. **21**, 181 (2010).
[19] N. J. Mottram and C. Newton, University of Strathclyde, Department of Mathematics, Research Report 10, 2004 (unpublished).
[20] A. Rapini and M. Papoular, J. Phys. Colloques **30**, 54 (1969).
[21] M. Nobili and G. Durand, Phys. Rev. A **46**, R6174 (1992).
[22] F. Bethuel, H. Brezis, and F. Hélein, Calc. Var. Part. Diff. Eq. **1**, 123 (1993).
[23] R. Hardt, D. Kinderlehrer, and F. H. Lin, Commun. Math. Phys. **105**, 547 (1986).
[24] L. C. Evans, *Partial Differential Equations* (American Mathematical Society, Providence, Rhode Island, 1998).
[25] The Sobolev space $H_0^1(\Omega)$ is the subset of $H^1(\Omega)$ with zero trace on the boundary [14].
[26] C. Johnson and C. Johnson, *Numerical Solution of Partial Differential Equations by the Finite Element Method* (Cambridge University Press, Cambridge, UK, 1987), Vol. 32.
[27] R. Seydel, *Practical Bifurcation and Stability Analysis* (Springer Verlag, New York, 2010).
[28] See Supplemental Material at http://link.aps.org/supplemental/10.1103/PhysRevE.85.061702 for the evolution of these solutions along the D1, D2, R2-R1, and R4-R3 branches, as well as for the switching from D1 to R2 with the electric field on and off and the switching from R2 to D1 with the electric field on and off.
[29] V. L. Streeter, E. B. Wylie, and K. W. Bedford, *Fluid Mechanics* (McGraw-Hill, New York, 1998).
[30] A. Iserles, *A First Course in the Numerical Analysis of Differential Equations* (Cambridge University Press, Cambridge, UK, 2008).
[31] R. L. Wheeden and A. Zygmund, *Measure and Integral* (Dekker, New York, 1977).
[32] G. Lombardo, H. Ayeb, and R. Barberi, Phys. Rev. E **77**, 051708 (2008).
[33] J. Hake, A. Logg, and G. N. Wells, DOLFIN: A C++/Python Finite Element Library, [https://launchpad.net/dolfin].
[34] S. H. Strogatz, *Nonlinear Dynamics and Chaos: With Applications to Physics, Biology, Chemistry, and Engineering* (Addison-Wesley, Reading, MA, 1994).
[35] F. Gomes and D. Sorensen, ARPACK++, [http://www.ime.unicamp.br/chico/arpack++/].